Applied Computing and Geosciences 12 (2021) 100073

Contents lists available at ScienceDirect

Applied Computing and Geosciences

journal homepage: www.sciencedirect.com/journal/applied-computing-and-geosciences

Forward modeling of magnetotellurics using Comsol Multiphysics

A. Li [1], S.L. Butler [*,2]

Department of Geological Sciences, University of Saskatchewan, Saskatoon, SK, S7N 5E2, Canada

ARTICLE INFO

Keywords:
Magnetotellurics
Comsol multiphysics
Complex crater
Geomagnetically induced curent
Tipper

ABSTRACT

Magnetotellurics is an electromagnetic geophysical method that has been widely used to study structures in Earth's subsurface. Numerical modeling of magnetotellurics is important for survey design, inversion, geological interpretation and many other aspects of geophysical studies. For example, modeling a subsurface conductive body in terms of its conductivity, geometry and dipping angle would yield substantial information on the phase response and sensitivity in an MT survey. While there are many different modeling techniques, the finite element method is most commonly used. In this effort, we present magnetotelluric models of layered Earth, uplift structures, auroral electrojets, and geomagnetically induced currents in power-line skywires using the commercial finite-element package Comsol Multiphysics. The AC/DC module in Comsol can be used to solve Maxwell's equations in the quasi-static limit for modeling the magnetotelluric response. One of the advantages of Comsol modeling is its Graphical User Interface (GUI), which allows users to solve complex single or multiphysics problems in a meshed domain. The use of Comsol also reduces the need for sophisticated computer coding when solving partial differential equations such as Maxwell's equations. In the effort presented here, we first discuss model validation for layered Earth geometries. We then present two examples of magnetotellurics modeling in impact crater and geomagnetically induced current studies. Numerical results were compared with analytical solutions or benchmark results whenever possible.

1. Introduction

Magnetotellurics (MT) is a frequency domain electromagnetic technique that uses naturally occurring electromagnetic fields to investigate the electrical conductivity structure of Earth (Vozoff, 1991). Natural sources of MT signals above 1 Hz result from lightning discharges and other meteorological activities worldwide. Other sources of signals below 1 Hz are due to interactions between the solar wind and the Earth's magnetosphere (Simpson and Bahr, 2005). Depth of investigation in MT exploration is controlled by the signal frequency and the ground resistivity (Chave and Jones, 2012).

As MT has been long applied in mineral (Swift, 1967), hydrocarbon (Keller, 1968) and lithosphere (Cantwell and Madden, 1960) exploration, it has become more important to perform numerical modeling prior to field work for survey planning and after field work to facilitate inversion. Examples of the importance of forward modeling prior to survey design and field campaigns are discussed in Jones and McNeice (2002); Queralt et al. (2007). One of the ways to numerically model MT is by solving the Helmholtz equations (McNeill and Labson, 1991) using the finite element (FE) method (Ansari and Farquharson, 2014). Ansari et al. (2020) have specifically developed FE algorithms for the magnetotelluric method. Some classic benchmark examples of MT modeling are given by (Zhdanov et al., 1997). In this contribution, we present examples of MT models created using a commercial package - Comsol Multiphysics.

Comsol Multiphysics (Comsol, 2014) is a finite element software that solves partial differential equations through a GUI platform. An advantage of modeling using Comsol is its simplicity in the user interface, which helps reduce sophisticated computer coding. The other advantage of Comsol is its flexibility in modeling complex geometries and coupling different physics. Comsol also has many built-in tools for post-processing data, which allows easy examination of various quantities. Examples of the use of Comsol in modeling electromagnetics with galvanic, loop and plane wave sources are given in Butler and Zhang (2016). In the present study, line currents and conductive boundaries were easily added. Also, if the ground resistivity changed because of the

* Corresponding author.
E-mail addresses: ang.li@usask.ca (A. Li), sam.butler@usask.ca (S.L. Butler).
[1] Contributed to manuscript text. Performed all calculations and quantitative analysis.
[2] Contributed to the manuscript text, revision and scientific analysis.

https://doi.org/10.1016/j.acags.2021.100073
Received 7 April 2021; Received in revised form 3 November 2021; Accepted 3 November 2021
Available online 12 November 2021

movement of fluids or changes in temperature, fluid flow or thermal models could be easily coupled to the MT model. Although the finite element method has become widely used in the application of MT modeling using different computer programs and software, Comsol Multiphysics has not been widely used in MT studies. Häuserer and Junge (2011) used Comsol to forward model MT with 3D structure representing the ground in the region of the Rwenzori Mountains and were able to get a good fit with their field measurements. Comsol-based MT forward models were used to investigate the effects of a narrow straight on MT measurements (Gonzalez-Castillo et al., 2015) while González-Castillo et al. (2015) modeled the tipper vectors in southern Spain. Lower and Junge (2017) used an MT Comsol forward model to study the effects of anisotropy in a conductive anomaly on the measured phase tensor and tipper vectors. Effects of electrical anisotropy and coast lines were investigated using Comsol MT models by (Cembrowski and Junge, 2018) while Liu et al. (2019) used Comsol forward modeling to investigate the contribution of electrical anisotropy to the MT signal measured in North-West China. Hering et al. (2019) used Comsol forward modeling of 1 and 2D resistivity structures with anisotropy to demonstrate the effectiveness of apparent resistivity tensors and Gonzalez-Castillo et al. (2019) used Comsol MT forward models to quantify the effects of seawater on MT measurements in Tierra del Fuego. For modeling results of various electromagnetic geophysical methods discussed in Butler and Zhang (2016), an example of an MT model was presented and compared to the benchmark result from Zhdanov et al. (1997). Another example of an MT model was given in the Comsol application gallery (Comsol, 2014). A few other examples of modeling the geomagnetically induced current in powerlines were discussed by Matandirotya et al. (2015).

Terrestrial impact structures have been studied using magnetotellurics (Zhang et al., 1988; Mareschal and Chouteau, 1990; Masero et al., 1994, 1997; Unsworth et al., 2002; Campos-Enriques et al., 2004; Adepelumi et al., 2005; Witherly et al., 2010). These structures typically contain fractured rocks, which have lower resistivity than undisturbed surrounding layers, and fractures may result in detectable conductive anisotropy.

Geomagnetically induced currents (GIC) are currents in conductors in the ground and on the ground surface, driven by changing magnetic fields in Earth's upper atmosphere. While GIC in the ground cause the signal measured by the magnetotelluric method, GIC in man-made conductors such as electrical power transmission lines and pipelines are hazards to infrastructure (Bowles-Martinez and Schultz, 2019). Additionally, GIC in man-made conductors may interfere with magnetotelluric studies (Bonner and Schultz, 2017).

In this effort, we first briefly review the theory describing the magnetotelluric method. We then describe our finite element model and its implementation in Comsol. Our model imposes magnetic fields on the outer boundaries that are determined from analytical solutions for fields in a layered Earth and these act as the forcing in the model. Model validation for magnetotelluric signal propagation in a layered Earth is then presented. Numerical results of the propagating magnetic field and electric field are compared with the analytical formulas from McNeill and Labson (1991). We then present MT modeling for impact structure studies and we compare numerical results with MT field results at a crater to constrain the degree of uplift. Finally, we present modeling of the induced currents in the ground due to an auroral electrojet and then of GIC and its flow in powerline skywires using Comsol. This modeling study demonstrates the ability in Comsol to model thin conductors using effective boundary conditions. By fitting model results for the current induced in the ground as a function of skin depth and wire length, we derive an expression for the distortion expected from a skywire-protected powerline.

2. Theory and method

For modeling Ampere's law in the frequency domain (Griffiths, 1999), the Magnetic Fields (mf) interface from the AC/DC module of Comsol was used. Ampere's law in the frequency domain as solved by Comsol reads:

$$\mathbf{H} = \frac{1}{\mu_0}\nabla \times \mathbf{A}, \qquad \mathbf{E} = -i\omega\mathbf{A} \qquad \nabla \times H + \left(i\omega\sigma - \omega^2\varepsilon_0\right)\mathbf{A} = \mathbf{J_e}, \tag{1}$$

where i is the imaginary unit, ω is the angular frequency, σ is the electrical conductivity and ε_0 is the electrical permittivity of free space. Here $\mathbf{H}$ is the magnetic field, $\mathbf{A}$ is the magnetic vector potential and $\mathbf{J_e}$ is the external current density which is 0 for all of our simulations. Note, this formulation of Maxwell's equations uses a gauge in which the scalar potential is 0 so only inductive sources can be modeled. In all of our simulations, we assume that the magnetic permeability and electrical permittivity are equal to the values in a vacuum. The relationship between the current density and the electric field is given by

$$\mathbf{J} = (\sigma + i\omega\varepsilon_0)\mathbf{E}. \tag{2}$$

Equation (1) is solved for the real and imaginary parts of the three components of the magnetic vector potential. The default discretization for the Magnetic Fields interface is used which consists of quadratic element while linear and cubic elements could also have been chosen.

In low frequency geophysics, such as magnetotellurics, the term representing the displacement current ($\omega^2\varepsilon_0$) is generally much smaller than the term describing the conductive current ($i\omega\sigma$). This is also known as the quasi-static limit of electromagnetic geophysics (McNeill and Labson, 1991). In our Comsol-based model, the displacement currents are included even though they are very small. A Cartesian coordinate system is used for modeling electromagnetic propagation in a layered Earth. Fig. 1 shows the geometry used as well as the wave propagation direction and the orientation of the magnetic field. The excitation of the model is achieved by enforcing a tangential magnetic field $\mathbf{H_0}$ on all of the outer domain boundaries, namely

$$\hat{n} \times \mathbf{H} = \hat{n} \times \mathbf{H_0}. \tag{3}$$

with

$$\mathbf{H_0} = \begin{bmatrix} -H(x,y,z)\sin\alpha \\ H(x,y,z)\cos\alpha \\ 0 \end{bmatrix}, \tag{4}$$

where α is the counterclockwise angle between the horizontal component of the wave propagation and the x-axis. the symbol H represents the analytical solution for the magnetic field for a layered conductivity structure.

The analytical expression for the magnetic field due to a plane wave source in and above layered ground is given by McNeill and Labson (1991):

$$H_m(x,y,z) = (a_m e^{-u_m z} + b_m e^{u_m z}) e^{-i\lambda(x\cos\alpha + y\sin\alpha)}, \tag{5}$$

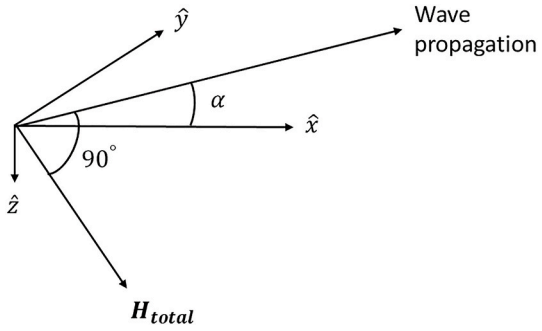

Fig. 1. Schematic diagram of the electromagnetic wave propagation. Angle α is the counter-clockwise angle between the x-axis and the propagation direction.

and the electric field given by

$$E_{mx}(x,y,z) = \frac{u_m}{\sigma_m + i\omega\varepsilon_0}(a_m e^{-u_m z} - b_m e^{u_m z})e^{-i\lambda(x\cos\alpha + y\sin\alpha)}. \quad (6)$$

Index $m = 0$ indicates the air layer and indices $m = 1, 2, \ldots$indicate ground layers of increasing depth. The magnetic field, $H(x, y, z)$ is made up of the various H_m in the m layers. In addition, $u_m = \sqrt{\lambda^2 - \kappa_m^2}$, $\kappa_m = \sqrt{-i\omega\mu_0\sigma_m}$ and $\lambda = \kappa_0 \sin\theta_i$. The angle of incidence θ_i is the angle at which the wave impinges the ground surface and is set to be $\theta_i = \pi/2 - \pi/40$ in the simulations shown here (Butler and Zhang, 2016). Coefficients a_m and b_m are determined from boundary conditions at each layer interface, namely the continuity of the tangential electric field and the tangential magnetic field (McNeill and Labson, 1991). An explicit calculation of the analytical expression for the wave equation over a three-layered earth is presented by Li (2020). Note that the coefficient a_0 represents the incoming wave amplitude and can be arbitrarily set to be 1.

All simulations were run using COMSOL Multiphysics 5.4 on a computer with 2 processors Intel(R) Xeon(R) CPU E5-2643 0 at 3.30 GHz, and with 128 GB of RAM and a 64 bit operating system. Comsol gives the number of degrees of freedom as an estimate of the size of the numerical problem. Degrees of freedom is equal to the number of nodes times the number of dependent variables. For the current problem, quadratic tetrahedral elements were used and there are six dependent variables corresponding to the real and imaginary parts of the three components of the magnetic vector potential. The number of nodes is roughly 1.4 times the number of elements and so the number of degrees of freedom is roughly 8.4 times the number of elements. The default settings for the solver in 3D for the Magnetic Fields module were used which consisted of using the BicGStab (Van der Vorst, 1992) iterative solver using right preconditioning. Comsol allows users to choose from a number of iterative and direct solvers. Although we did not use them, Comsol also gives the option of using swept meshes and adaptive meshing.

The importance of resolution in numerical modeling was discussed by Butler and Zhang (2016). The distance over which the field is attenuated can be estimated by the skin depth:

$$\delta = \sqrt{\frac{2\rho}{\mu_0\omega}}, \quad (7)$$

where ρ is the corresponding layer's resistivity and μ_0 is the electrical permeability of free space. To satisfy the resolution in frequency domain studies, the mesh is defined such that there are at least a few element edges over one skin depth unit. Comsol allows users to break domains into different volumes and mesh at different resolutions within domains. Higher resolution on boundaries with specified element growth rates into the domain can also be used. Mesh quality can be monitored using various measures including skewness, volume versus circumradius and condition number. It is also equally important that the domain size is sufficiently large that the outer boundary conditions are not significantly affecting the solution (Butler and Zhang, 2016). Therefore, the domain outer boundaries need to be at least 2 skin depths away from the point of interest to minimize the boundary effects. As can be seen from equation (7), the necessary mesh resolution depends on frequency and resistivity. In COMSOL Multiphysics, the mesh size can be set as a function of skin depth, which is automatically adjusted according to the different parametrizations. Typically, we set the mesh element size to be a quarter of a skin depth in the corresponding layer.

Increasing mesh resolution results in higher quality solutions but longer run times and greater RAM usage. In all the simulations shown here, the maximum mesh element sizes range from 300 m to 40 km, the model run times range from 40 s to 2.5 h, and the memory usages range from 4 GB with 65823 elements to 70 GB with 1674809 elements.

3. Model validation for a layered earth

In all of the simulations presented, a rectangular prism is chosen as the model domain. The prism includes regions that represent air of very low conductivity ($z < 0$ km) and ground ($z > 0$ km). Each ground layer is assumed to be isotropic and homogeneous. The electrical permittivity and the magnetic permeability within the layers are assumed to be those of free space, 8.85×10^{-12} F/m and $4\pi \times 10^{-7}$ H/m respectively.

As a preliminary assessment, numerical solution of a homogeneous Earth model was compared with the corresponding analytical solution. Good agreement between the two was found and is discussed in Li (2020). Here we present the simulated results for a three-layered earth model at a frequency of 0.1 Hz. The simulation took 283 s and used 4055966 degrees of freedom, which required 18.79 GB of physical memory.

Although 1D resistivity structure is used for calculation, the numerical models were fully 3D. It is discussed by Butler and Zhang (2016) that since the analytical solutions for the magnetic field are specified on the boundaries for a layered Earth model, there should be no lateral variations in the magnetic or the electric field inside the domain so that the magnetic field calculated along a vertical profile at the center of the domain should be exactly the same as specified on the boundaries. Fig. 2 shows the mesh construction for a three-layer Earth model. Regions $0 < z < 5$ km, $5 < z < 15$ km and $z > 15$ km represent layers with resistivities of 100 Ωm, 10 Ωm and 1 Ωm respectively. The region above 0 km is air and its resistivity is set to be 10^9 Ωm. While this resistivity is significantly less than the real value of air, it is sufficiently large that it is not affecting the conduction in the ground. In Fig. 3, we show the comparison between the analytical (solid line) and the numerical (circles) solutions of the real and imaginary parts of the horizontal magnetic field H_y, horizontal electric field E_x and vertical electric field E_z along a vertical profile at the center of the model. We clearly show that the analytical and the numerical solutions match well. There is a small mismatch in the real part of E_x which may be due to the assumption of 0 conductivity in the analytical model while it is small but non-zero in the numerical model. The discontinuities of the slope of both the real and the imaginary parts of H_y are observed at each of the layer interfaces as well as the discontinuity in E_z at the ground surface. Since the horizontal magnetic and the horizontal electric field at the ground plane ($z = 0$) can be obtained numerically (by Comsol) and analytically (from equation (5)), we can calculate the apparent resistivity and the phase as a function of frequency:

$$\rho_a = \frac{1}{\mu_0\omega}\left|\frac{E_x}{H_y}\right|^2, \qquad \varphi = \arctan\frac{\Im(E_x/H_y)}{\Re(E_x/H_y)}, \quad (8)$$

where $\Im$ and $\Re$ are the imaginary and real operators. Table 1 shows a comparison of the analytical and numerical results of the horizontal magnetic field (H_y), the horizontal electric field (E_x), the apparent resistivity (ρ_a) and the phase (φ) on the ground plane ($z = 0$). Again, both of the results match well. Similarly, simulations can be run at a range of different frequencies to model the naturally occurring electromagnetic signals. Fig. 4 shows a comparison of the analytical and numerical results of the (a) apparent resistivity and (b) phase of the same three-layered model from 0.01 Hz to 100 Hz. The percent root-mean-square (RMS) misfit between the analytical and numerical solutions for the three layer model is calculated to be less than 0.1 percent.

4. Modeling a subsurface uplift

The use of MT in detecting subsurface uplift features, such as those caused by meteorite impact events, has been studied in the past. Studies of the Chicxulub crater near the Gulf of Mexico using magnetotellurics were presented by Unsworth et al. (2002) and Campos-Enriques et al. (2004). Another study on a suspect complex impact structure at Pasfield Lake, Saskatchewan, Canada was carried out by Witherly et al. (2010).

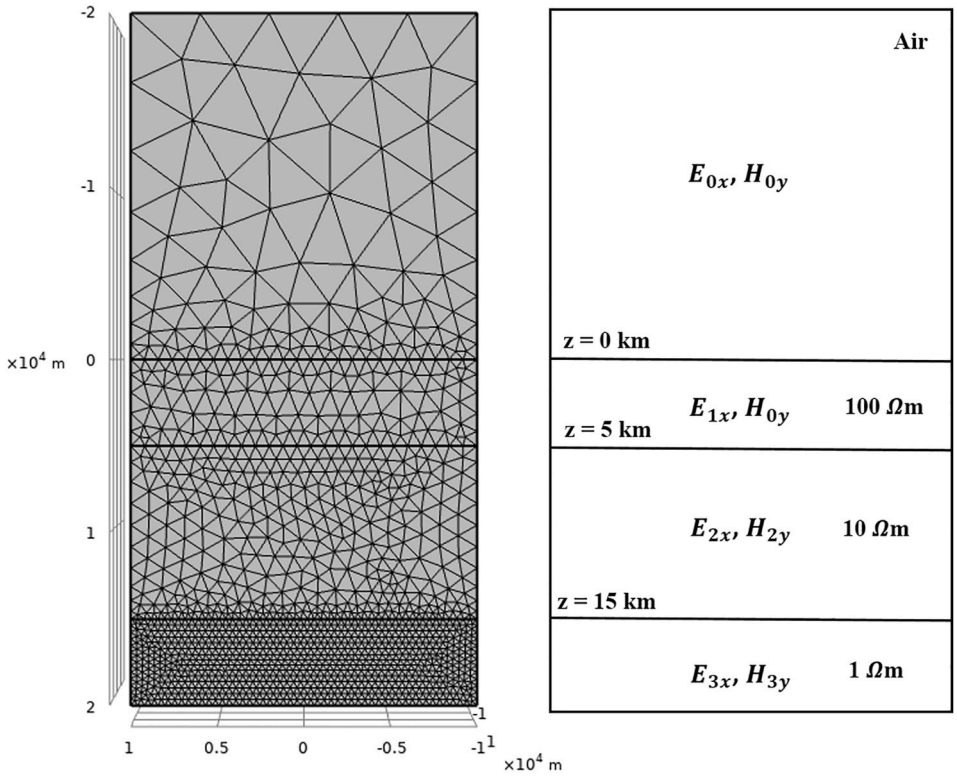

Fig. 2. Three layered model mesh and geometry with depth and resistivitiy values indicated.

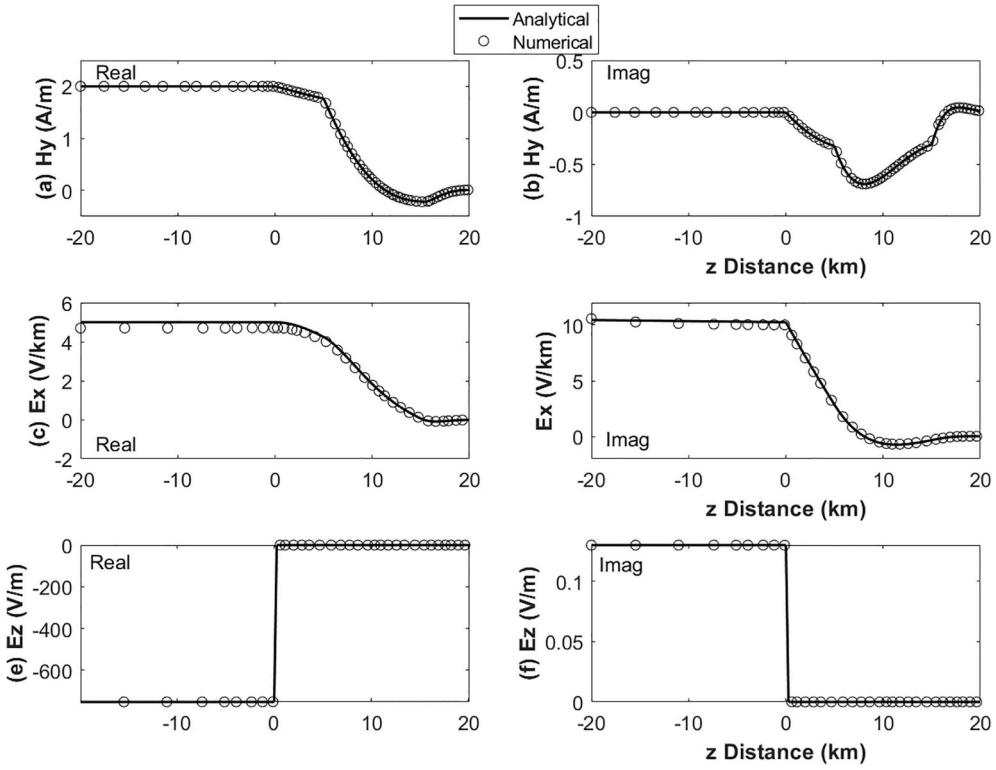

Fig. 3. Comparison of the analytical (solid line) and the numerical (circles) solutions of the (a) real and (b) imaginary components of H_y, E_x and E_z along a vertical profile at the center of the model at 0.1 Hz. Regions $0 < z < 5$ km, $5 < z < 15$ km and $z > 15$ km represent layers with resistivity 100 Ωm, 10 Ωm and 1 Ωm respectively. The region $z < 0$ km represents air with a resistivity of 10^6 Ωm.

Table 1
Comparison of the analytical and numerical results of the horizontal component of the magnetic field (H_y), the electric field (E_x), the apparent resistivity (ρ_a) and the phase (φ) on the ground surface ($z = 0$) at 0.1 Hz.

	Analytical	Numerical
H_y (A/m)	$1.999–3.468 \times 10^{-4}i$	$1.999–5.447 \times 10^{-4}i$
E_x (V/m)	$0.005004 + 0.01025i$	$0.005004 + 0.01025i$
ρ_a (Ωm)	41.22	41.22
φ (°)	63.99	63.99

When studying the structure and the extent of the impact region, gravity and reflection seismic are often used initially to interpret the characteristic concentric anomalies, such as a central uplift (Grieve, 2006). Electrical and electromagnetic techniques are less commonly used for investigating impact structures (Grieve, 2006). Nevertheless, Pilkington and Grieve (1992) argued that a possible detectable signature of the impact structure is the presence of fluid in the impact-induced fractures and pore spaces, which could lead to a difference in the subsurface resistivity that can be interpreted by electrical (shallow) or electromagnetic (shallow or deep) techniques.

The characteristic morphology of a complex impact structure, as described in Grieve (2006), is the central structurally uplifted area surrounded by a down-faulted annular trough, with no disturbance of the deep horizons. To simulate the effect of a central uplift in a layered earth model numerically, model parameters are derived from the inverted magnetotelluric field data collected at a complex crater near Elbow, Saskatchewan, Canada.

The Elbow structure (50°59′N, 106°43′W), named after the nearby town of Elbow, is located in south central Saskatchewan on an elbow of the south Saskatchewan river. The structure is 8 km in diameter and circular in plan, with a central structurally uplifted area of fractured and brecciated target rocks surrounded by a ring depression (DeMille, 1960). Magnetotelluric data were collected across 7 stations using Phoenix MTU-8A receivers in the fall of 2019 (Fig. 5). Galvanic distortion analysis including static shift correction was done following Bibby et al. (2005) and Jones (1988). Strike and dimensionality analysis were done using the phase tensor decomposition method (Caldwell et al., 2004). The measured tipper is too small to reflect subsurface variations. Based on the phase tensor calculation, geological structures are found to be 1D dominant hence data are treated as 1D and 1D inversion is justified. Data processing including cross power editing was done using *EMpower* (Phoenix, 2019). Galvanic distortion and phase tensor analysis were carried out using the open source software *MTpy* (Kirkby et al., 2019; Krieger and Peacock, 2014). Although the data were dominantly 1D, there was a weak indication of a strike direction of 10° east of north at 1 Hz and data were rotated into TE And TM models accordingly. The apparent resistivity and phase determined for the TE and TM models were very similar and so only one is plotted. Fig. 6 (a) and (b) show the apparent resistivity and phase sounding at station 'elbow1′ in the Elbow region. Fig. 6 (c) shows the inverted three-layer model using the algorithm of McLeod (2016). The inverted parameters (layer resistivities and depths) are then used in our Comsol-based model of a layered Earth. Numerical results of the layered earth model derived from the inverted parameters are shown in Fig. 6 (a) and (b). The apparent resistivity and phase calculated using Comsol show good agreement with those predicted from the inverse model. Fig. 7 shows pseudo-sections of the TE apparent resistivity and phase data collected at the impact region. Fig. 8 shows the major and the minor axes of the measured phase tensor ellipses for all stations. Although there is some variability of the phase near the surface, the data mostly indicates a layered geometry with no discernible uplift feature. The lack of this feature is further investigated using Comsol-based modeling.

To model a 3D central uplift structure, a Gaussian bulge can be constructed by defining a parametric surface in Comsol. The equation that describes a Gaussian bulge is given by

$$G(x, y) = -Ae^{-(x^2+y^2)/c^2}, \tag{9}$$

where A and c define the vertical amplitude and the width of the uplift. As shown in Fig. 9, the parametric surface is built on the interface between the second and the third layer and has an amplitude of 1 km and a width of 2 km. Extremely fine mesh is used at the parametric surface and normal mesh is used elsewhere where "Extremely fine" and "normal" are

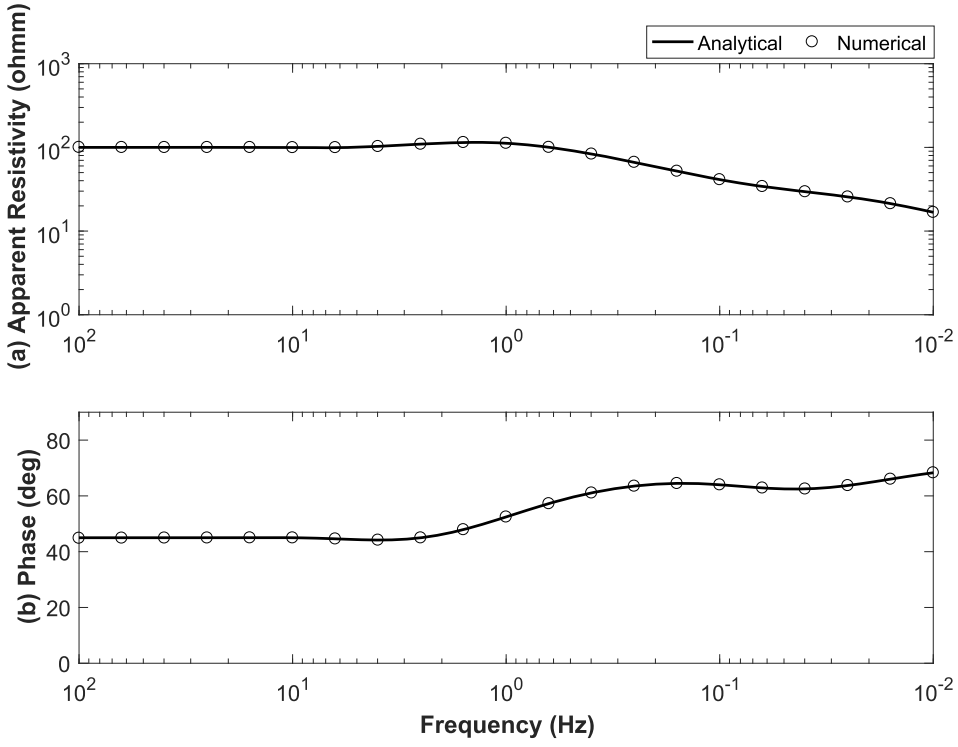

Fig. 4. Comparison of the analytical (solid line) and the numerical (circles) solutions of the (a) apparent resistivity and (b) phase for the three-layered earth model.

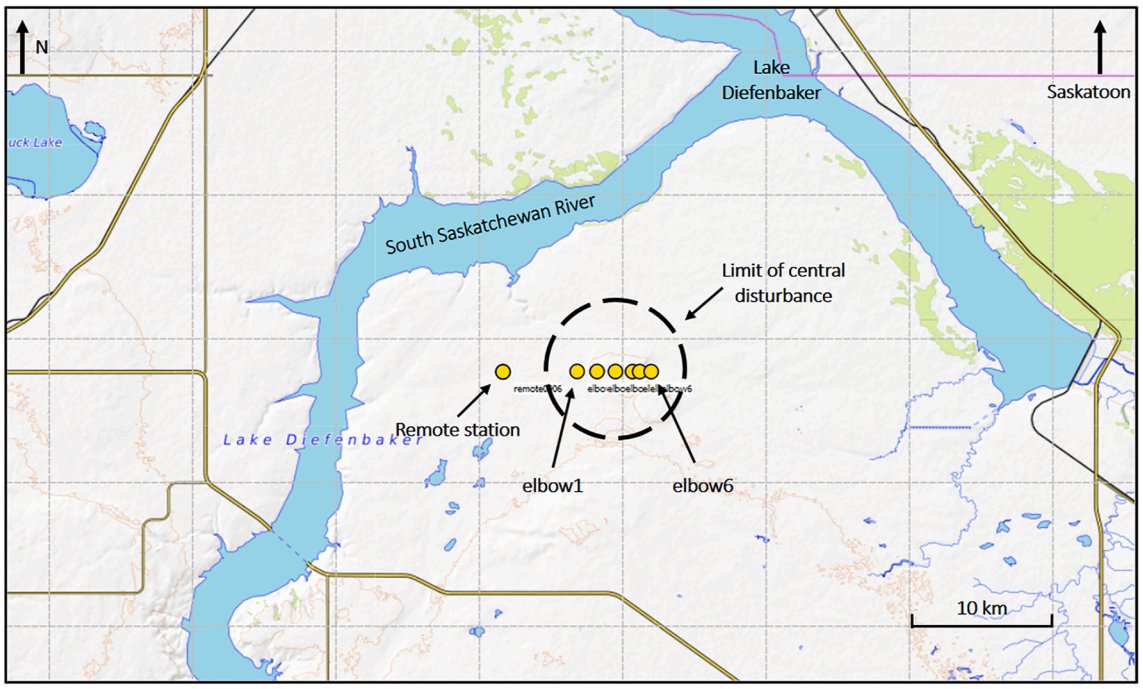

Fig. 5. MT survey map at the Elbow impact region. The disturbance limit is shown by dashed circle. Remote station and survey stations are shown by yellow circles.

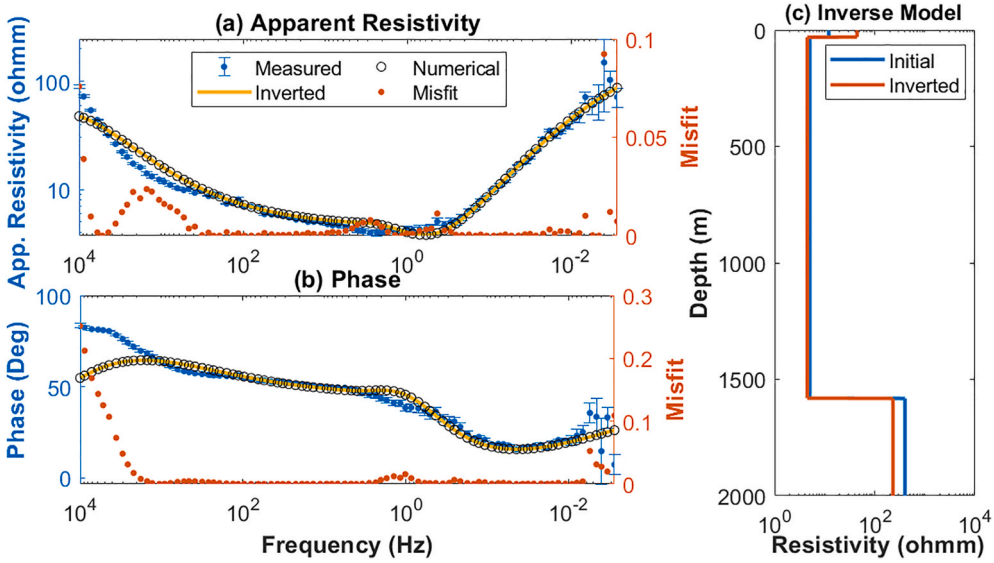

Fig. 6. 1D Inversion of the TE mode of magnetotelluric sounding measured at station 'elbow1' in the Elbow impact region. The measured (a) apparent resistivity and (b) phase (with error bars) are shown in blue dots. The inverted results are shown as yellow lines and numerical results are shown as black circles. The inverse model is shown in (c) and the misfit between the measured and the inverted data are shown in red dots in (a) and (b).

Comsol mesh settings. The frequency domain study used 0.0001 Hz to 10 kHz with 5 steps per decade spacing. These different frequencies were investigated using a 'parameter study'. The simulation took 291 s and used 3.43 GB of RAM and 325706 degrees of freedom. Fig. 10 shows the TE mode of the apparent resistivity pseudo-section along the x-axis from the Comsol simulation. The effect of the central uplift can be seen as an upward deflection in the resistivity contours for periods of 80 s or less. More simulations were run to investigate the effect of varying uplift amplitudes on the apparent resistivity response. Fig. 11 shows the simulated apparent resistivity pseudosection and Fig. 12 shows vertical profiles of apparent resistivity at $x = 0$. Both figures show that when the uplift amplitude was 500 m and less, the uplift became difficult to detect from the resistivity profile. As seen from the modeling results, the lack of an uplift feature in the collected data (Fig. 7), indicates that the uplift in the Elbow region was probably less than 500 m in amplitude.

5. Modeling GIC flow in overhead skywires

Geomagnetically induced current (GIC) results from rapid changes of the Earth's geomagnetic field due to magnetic disturbances. According to Faraday's law and Ohm's law, the change in the magnetic field induces an electric field, which drives GIC's in the ground (Oliveria and Ngwira, 2017). Currents driven by the induced electric field in the ground can flow in powerline skywires due to a voltage difference at both ends (Ingham et al., 2017) as well as due to effects of induction due to changing magnetic fields between the skywire and ground and due to

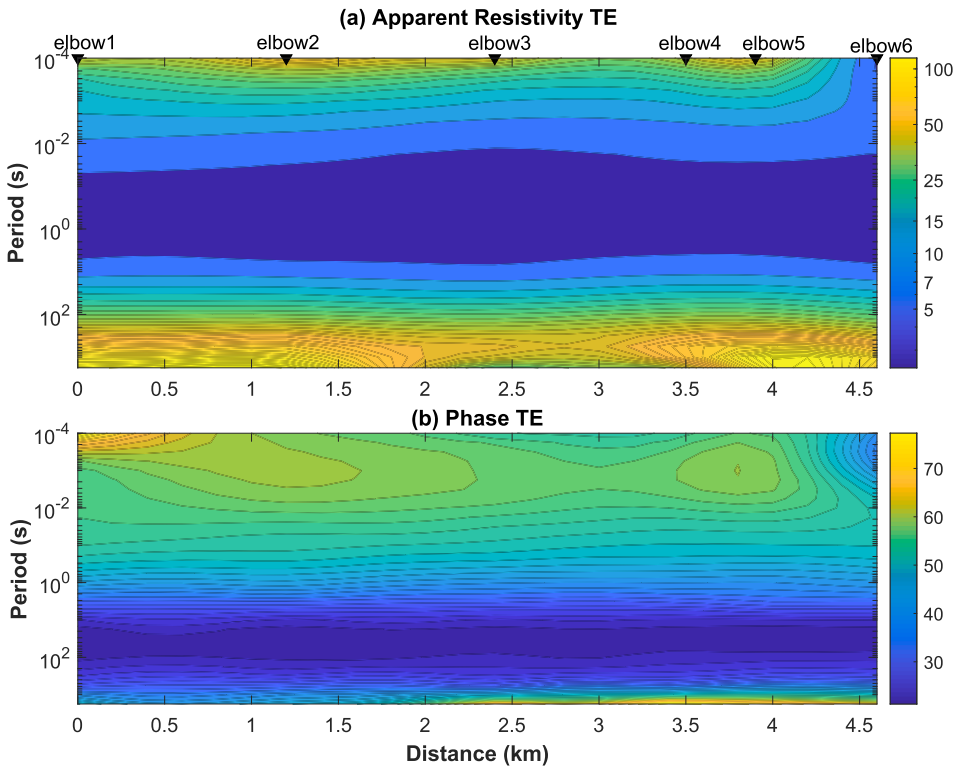

Fig. 7. Pseudo-section of the TE mode of (a) apparent resistivity and (b) phase from field measurements. Station names 'elbow1' through 'elbow6' are indicated on the graph. Colorbars in (a) and (b) are in units of Ωm and degrees.

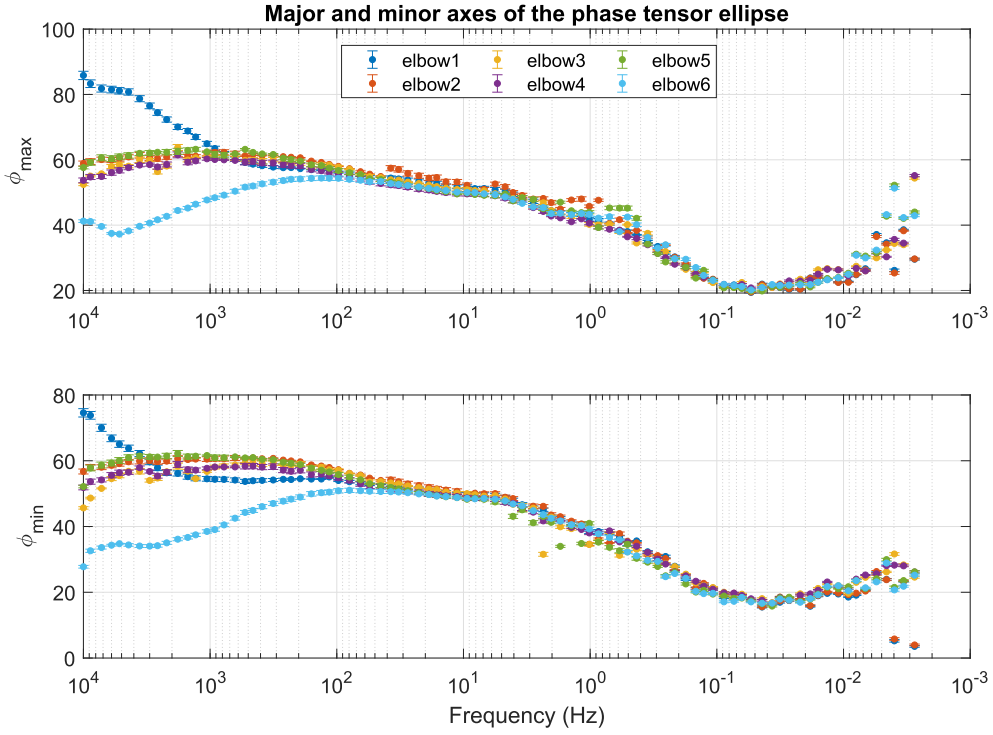

Fig. 8. Comparison of the major and minor axes of the phase tensor ellipses at different stations.

induced currents within the skywire itself. The powerline towers are grounded and the skywires are uninsulated and connected to the ground at the pylons for lightning protection.In magnetotelluric measurements, a quantity that defines the vertical component of the magnetic field divided by the horizontal magnetic field is referred to as the "tipper" (Telford et al., 1990; Vozoff, 1991). GIC flow in overhead skywires can cause an anomalous tipper. We use Comsol to carry out numerical modeling of GIC flow in skywires in order to better understand the degree of interference caused by powerline skywires on measured MT tipper values and to provide recommendations on needed distances from

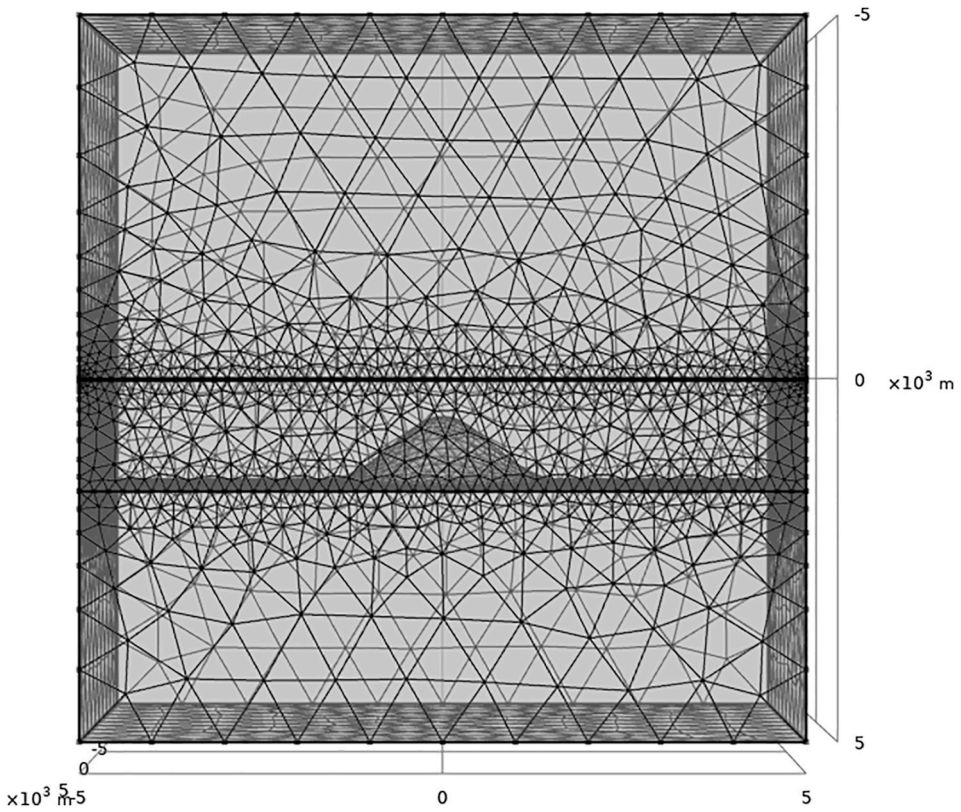

Fig. 9. Geometry and mesh construction for the fully 3D uplift model in Comsol. The domain size is 10 km by 10 km by 10 km. The uplift has a vertical amplitude of 1 km and a width of 1 km.

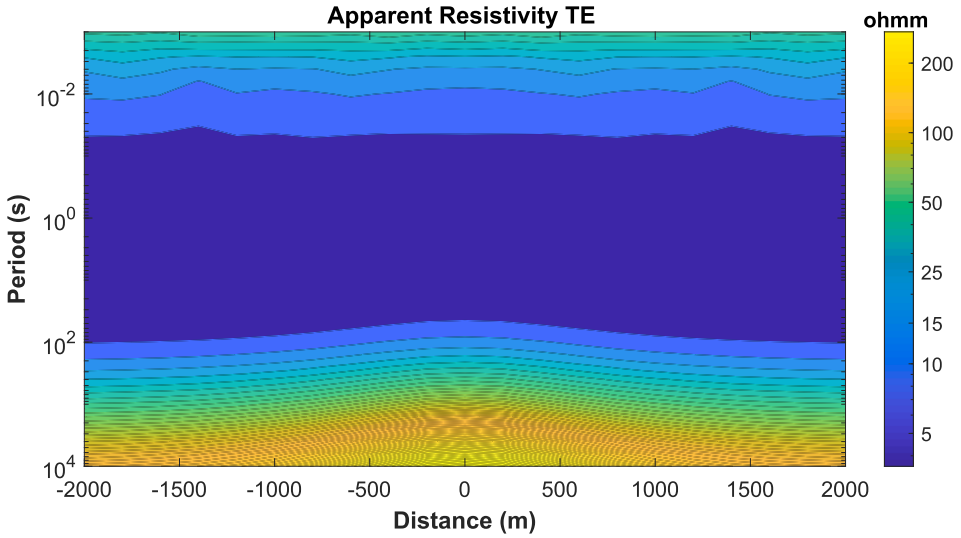

Fig. 10. Pseudo-section of the TE mode of apparent resistivity for an uplift with 1 km amplitude along the x-axis.

skywires.

5.1. Electrojet modeling

Before modeling GIC flow in an overhead skywire, numerical simulation of a slightly different model - an auroral electrojet is used as a benchmark comparison. Expressions for the electric and magnetic fields produced at the Earth's surface by an auroral electrojet (an infinitely long current) are presented as series expansions in Hermance and Peltier (1970); Pirjola (1998); Pirjola and Boteler (2002); Pirjola and Vilijanen (1998, 1999). A quantity called the "complex skin depth" is defined as

$$\delta_c = \frac{Z^*}{i\omega\mu_0}, \tag{10}$$

where Z^* is the complex impedance at the Earth's surface and is derived recursively from the underlying layers (Wait, 1981). Boteler and Pirjola (1998) presented a complex image method for analytically calculating the electric and magnetic field at the Earth's surface produced by an auroral electrojet. While the primary field is produced by the line current, a secondary current (image current) is induced in the ground at a

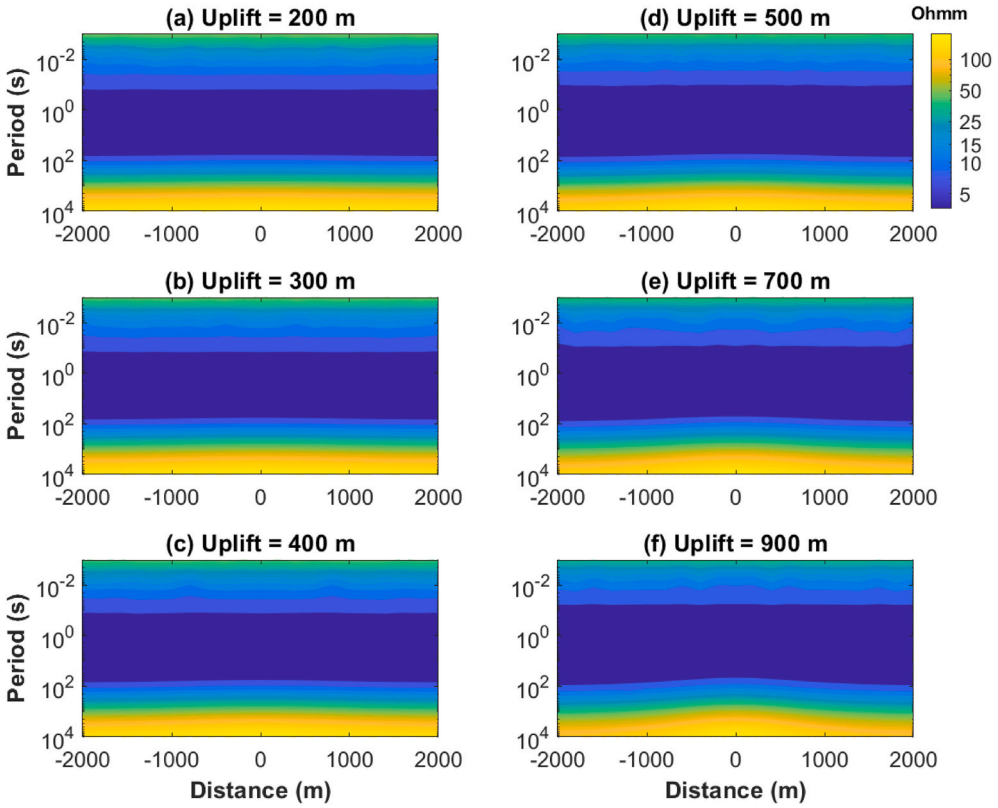

Fig. 11. Investigation of the effect of various uplift amplitudes on the apparent resistivity response: (a) $A = 200\ m$, (b) $A = 300\ m$, (c) $A = 400\ m$, (d) $A = 500\ m$, (e) $A = 700\ m$, (f) $A = 900\ m$.

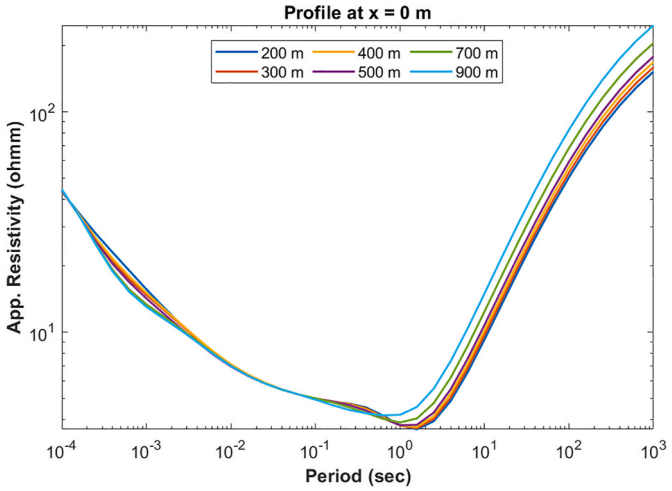

Fig. 12. Apparent resistivity response for the station at x = 0 m for models with different uplift amplitudes.

depth of $h + 2|\delta_c|$, where h is the height of the line current.

We model the electrojet as a line current which we specify by creating a straight line across the entire domain in geometry and specifying a harmonically varying current on that line. The boundary condition for the electrojet model sets the normal component of the magnetic field to zero and is implemented using the 'Magnetic Insulation' boundary condition in Comsol. As presented in Boteler and Pirjola (1998), the electrojet is specified at a height of 100 km and has a current of 10^6 A. The simulation took 6599 s and used 26119282 degrees of freedom and 66.86 GB of RAM. Fig. 13 is a vector arrow plot of the magnetic field in the air and in the ground produced by a line current at 100 km elevation and the currents induced in the ground. The image current in the numerical model is not specified but arises in the ground because of induction while the position of the image current predicted by the analytical theory is included on the diagram. The magnetic field lines produced by the primary current (at height h above ground) orient in the clockwise direction and those due to the image current (at depth $h + 2|\delta_c|$ below ground) orient in the counterclockwise direction. Comparison between the numerical results from Comsol and the benchmark results from Boteler and Pirjola (1998) for the various components of the electric and magnetic fields is shown in Fig. 14. Good agreement between the two can be seen. We also plot both the primary and total fields as calculated from the analytical expressions of Boteler and Pirjola (1998). The primary is the analytically derived field in the absence of a conducting Earth. It can be seen that the differences between the total field, as calculated from both the analytical expression and our numerical model, and the primary field are largest for the real parts of the vertical and horizontal magnetic fields, indicating that the effect of currents in the ground have the greatest impact on these quantities.

5.2. Calculating the GIC in the ground

In these calculations, the boundary condition of equation (4) was again used as the excitation in the model. The resulting electric and magnetic fields induce currents to flow in a conducting skywire and in the ground. To model the conducting skywire, a transition boundary condition is used to specify the skywire as a conducting surface that is geometrically thin but not electrically thin (Comsol, 2014). The transition boundary condition is described by the relationship of the electric field discontinuity and the induced surface current density of the two sides of the layer. For the results presented here, the skywire is set to have a conductance of 10^6 S. Different conductor resistivities were used for model testing and we found that these did not affect the results provided that the wire has a high conductance. In Fig. 15, the

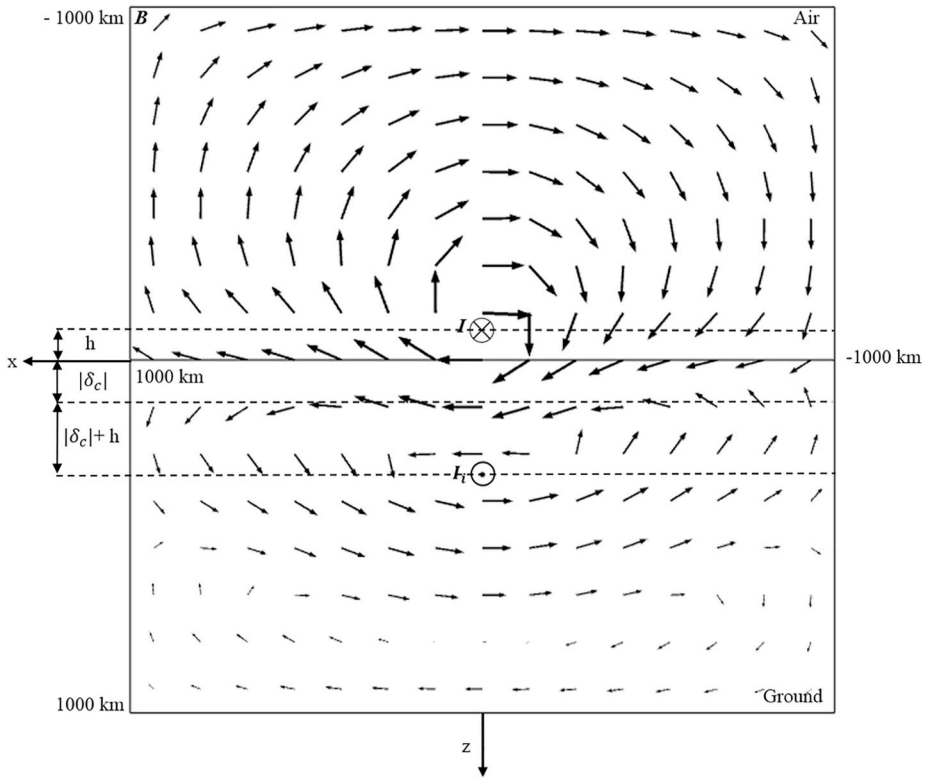

Fig. 13. Cross sectional view of the magnetic field lines produced by the primary current (into the page) and the secondary current (out of the page) from numerical modeling. The primary field I has a current of 1 million A and is at a height of 100 km above the ground surface. The secondary current (image current) I_i is at a depth of $h + 2|\delta_c|$ below the ground surface. Note that the image current is not specified in the numerical model but rather arises due to induction in the ground.

conducting wire is modeled at a height h, with the two ends fixed and grounded at (0, $-L/2$, 0) and (0, $L/2$, 0). The wire sits above a ground that is homogeneous. The height and the length of the skywire can be varied to study the corresponding effect on the induced magnetic field amplitude.

By defining a hemispherical surface centered at one of the grounding ends, the induced current in the ground can be calculated by integrating the current density on the surface of the hemisphere. The induced current in the ground is determined by the following surface integration:

$$I = \iint_S \mathbf{J}\cdot\hat{\mathbf{n}}da = \iint_S (J_x n_x + J_y n_y + J_z n_z)da, \tag{11}$$

where $\mathbf{J}$ is the current density in the ground calculated in Comsol using equation (2) and $\hat{\mathbf{n}}$ is the unit vector normal to the hemispherical surface. Induced currents in the ground are calculated for models with different skywire lengths. When the calculated currents are plotted against the model's complex skin depth normalized by the model's skywire length (Fig. 16), models with different skywire lengths, ground resistivities and frequencies are found to share a similar mathematical relationship. This was fitted as a power law with least squares regression:

$$I(\omega) = I_0\left(\frac{|\delta_c|}{L}\right)^{-1.0378}\left(\frac{H_0}{H_r}\right), \tag{12}$$

where I_0 has a value of $10^{0.8149}$ Amps, the model skywire length is given by L, the amplitude of the horizontal magnetic field that is imposed on the model boundaries is given by H_r and H_0 is the magnitude of the horizontal magnetic field at the ground surface in the absence of the skywire. The magnitude of the current is given by $I(\omega)$. For the results presented here, H_r and H_0 are roughly equal and H_r has a value of 2 A/m. Because the skywire is grounded, the current flowing in the wire equals the current induced in the ground. The good fit between the numerical model results and equation (12) indicates that the current is roughly inversely proportional to the skin depth.

For the skywire simulations, we define the TE and TM modes as those where the magnetic field of the incoming wave oscillates perpendicular and parallel to the skywire, respectively. We found that there was maximum coupling for the TE mode and so the largest effect of the skywire on the tipper while the TM mode was null coupled and there was no anomalous tipper. The results presented here will all be for the TE mode. It is generally true that the skin depth is much larger than the skywire height, so that the current in the ground is spread out and the magnetic fields are essentially due to the current in the skywire. To construct a simple, approximate, analytical model of the anomalous field due to the skywire that we can compare with the full Comsol-based numerical model, we can then approximate the magnetic field as that due to an infinite wire with current $I(\omega)$,:

$$H_z(\omega) = -\frac{I(\omega)}{2\pi}\frac{x}{x^2+h^2}, \qquad H_x(\omega) = -\frac{I(\omega)}{2\pi}\frac{h}{x^2+h^2}. \tag{13}$$

We note that equation (13) is based on the equation for an infinite straight wire and so we are additionally neglecting the edge effects of a finite wire in using equation (13). The maximum H_z is found at $x = h$ and has an amplitude of

$$H_z^{max}(\omega) = -\frac{I(\omega)}{4\pi h}. \tag{14}$$

Not only can we compute the induced current in Comsol, we can also predict the maximum vertical magnetic field using equations (12) and (14). Fig. 17 shows the numerical and the predicted H_z^{max} as a function of the normalized skin depth. Generally good correlations between the numerical solution and equation (13) are seen when $|\delta_c/L|$ is larger than or similar to 1 and this scaling is seen to extend to lower $|\delta_c/L|$ for larger values of L. However, when the skin depth decreases, the magnetic field

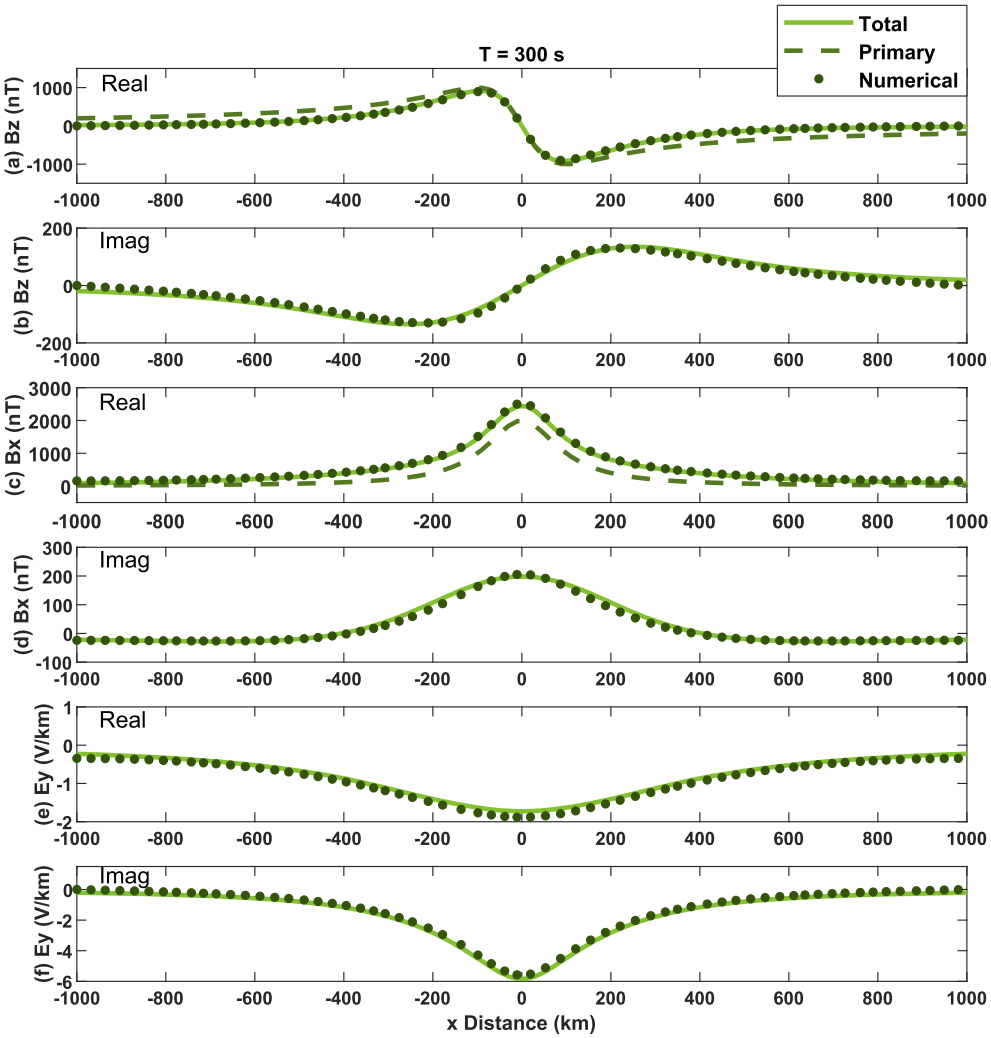

Fig. 14. Numerical result of the magnetic and the electric fields calculated along a profile orthogonal to the strike of the electrojet at the ground surface. The solid and dashed lines represent the analytical solutions of the total and primary fields from Boteler and Pirjola (1998). The simulation is with a frequency of 1/300 Hz.

is affected by both the current in the skywire and the current in the ground.

5.3. Effect on the tipper

In order to further develop the simple analytical model, we assume that most of the anomalous tipper is due to the current in the skywire itself. Using equation (13) we can calculate the approximate anomalous tipper value:

$$T_x = \frac{H_z}{H_x + H_0} = \frac{x}{h - \frac{2\pi}{I}(x^2 + h^2)H_0}. \tag{15}$$

By defining a length scale D as the distance from an infinite wire carrying current $I(\omega)$ where the H-field falls to H_0 we obtain

$$T_x = \frac{x}{h - (x^2 + h^2)/D}. \tag{16}$$

The length scale D can be written using equation (12):

$$D = \frac{I}{2\pi H_0} = \frac{I_0(L/|\delta_c|)^{1.0378}}{2\pi H_r}. \tag{17}$$

In the regime where $|\delta_c/L| > 1$, which is where the scaling is valid, then $h \gg D$. The fit extends to lower values of $|\delta_c/L|$ for larger values of L (Fig. 17). Additionally, the highest amplitude of the tipper occurs at a horizontal distance of

$$x_{max} = \pm\sqrt{h(h - D)}, \tag{18}$$

with an amplitude of

$$T_x^{max} = \mp\frac{D}{2\sqrt{h(h - D)}}. \tag{19}$$

Note that the maximum tipper value occurs at a distance of $x \approx h$ when $h \gg D$. Hence the maximum tipper value is

$$T_x^{max} = \frac{D}{2h}. \tag{20}$$

Because the length parameter D is a function of the normalized skin depth, T_x is dependent on both the resistivity of the ground and the length of the skywire. As we can see, T_x^{max} depends on the skywire height, the skywire length and the ground resistivity. The amplitude of T_x^{max} increases close to linearly with the skywire length (L) and decreases close to linearly with the skywire height (h). It also decreases as the square root of the resistivity of the ground.

Fig. 18 shows the magnitude of the tipper obtained using equation (16) and calculated using Comsol at 1 Hz and 100 Hz. We observe the maximum tipper magnitude occurs at $x \approx h$ for both frequencies. The fit

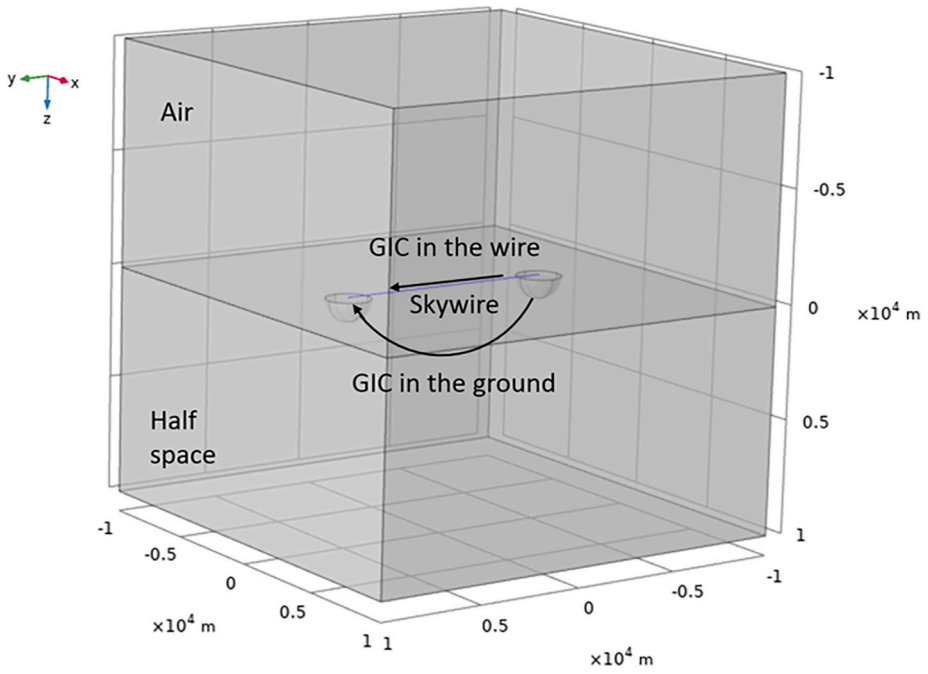

Fig. 15. Skywire model with air and half space layers. The skywire is grounded at both ends at the hemispheres and is at some height above the ground surface. Directions of the induced current flow in both the skywire and the ground are shown.

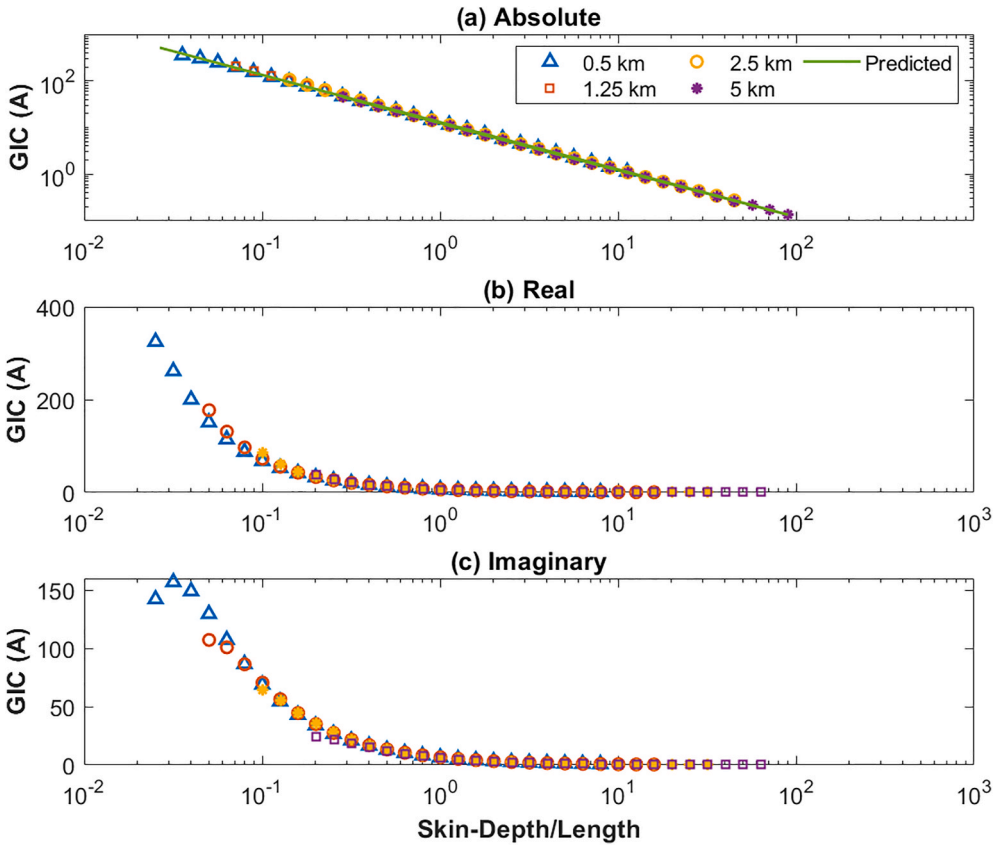

Fig. 16. Numerical calculation of the induced current in the ground produced by a skywire in the model. Absolute (a), real (b) and imaginary (c) parts of GIC are plotted as a function of the skin depth normalized by the skywire length. Fitted result for equation (12) is shown by the solid green line in (a). Symbols indicate model results of different skywire lengths. In this calculation, frequency is varied and the ground resistivity is fixed to be 1000 Ωm.

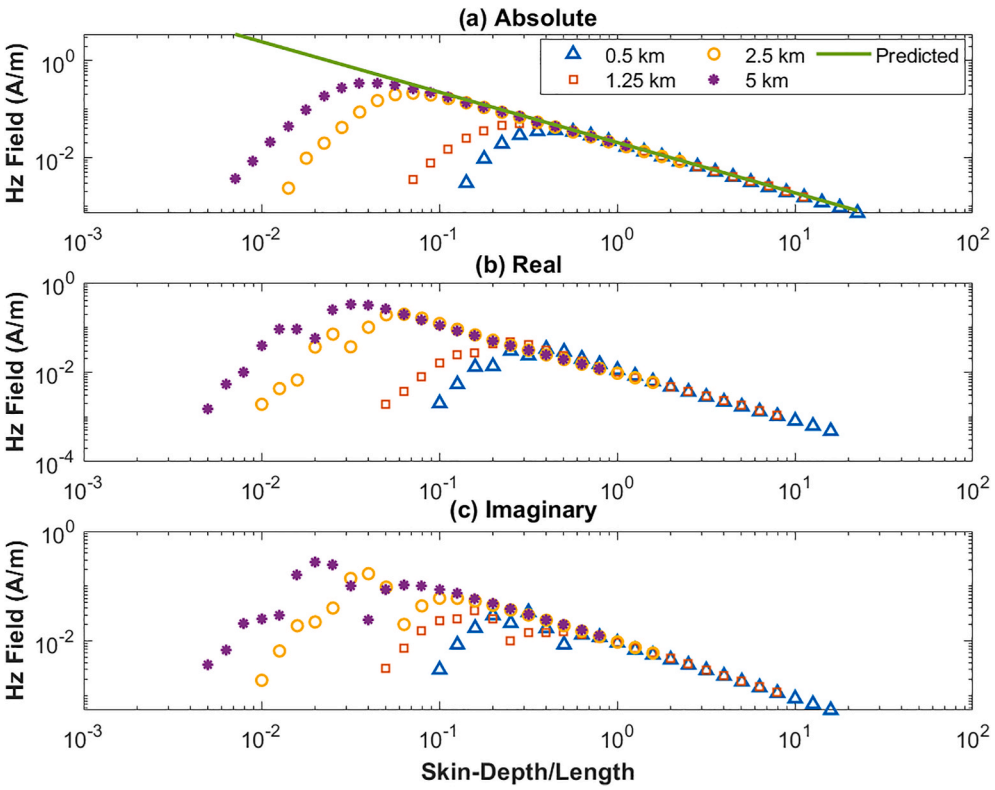

Fig. 17. The maximum value of the vertical component of the magnetic field H_z at the ground surface due to the induced current flow in the ground and skywire as calculated from our Comsol-based numerical model (symbols). Absolute (a), real (b) and imaginary (c) parts of the H_z are plotted as a function of the skin depth normalized by the skywire length. The solid line represents the predicted solution using the simplified model represented by equation (12) and equation (14). In this calculation, frequency is varied and the ground resistivity is fixed to be 1000 Ωm.

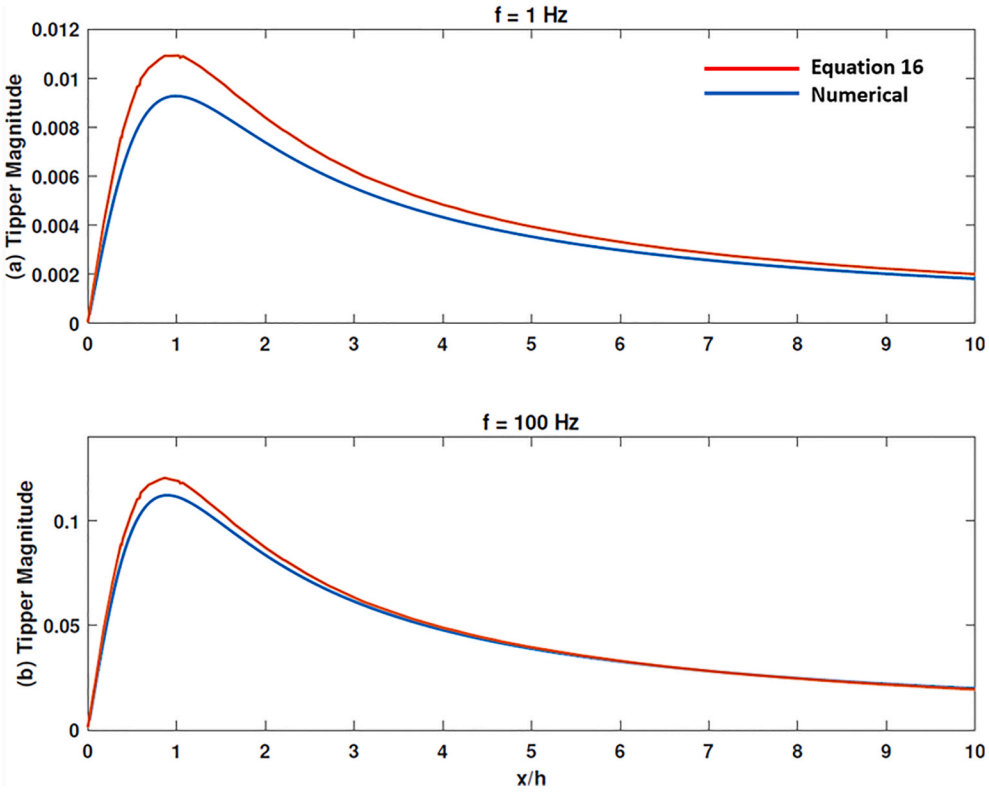

Fig. 18. Comparison of the tipper magnitudes plotted as a function of horizontal distance normalized by the skin depth. Respectively, red and blue lines indicate tipper magnitudes computed numerically and using equation (16) at (a) f = 1 Hz ($\delta_c = 7.96 \times 10^3 - 7.96 \times 10^3 i\ m$) and (b) f = 100 Hz ($\delta_c = 7.96 \times 10^2 - 7.96 \times 10^2 i\ m$). In this calculation, the skywire length and height are 10 km and 50 m, the ground resistivity is 1000 Ωm.

is sufficient for estimating whether the anomalous tipper from the grounded skywire will be problematic. We could also observe that the anomalous tipper magnitude gradually decreases as the observation points move away from the center of the source current. On the other hand, the fit between equation (16) and numerical solutions are not as good for frequencies higher than 1 kHz where the skin depth to length ratio is much less than 1. However, at these high frequencies, the amplitude of the anomalous tipper is usually small.

5.4. Recommendation for field work

With regards to MT field work near a powerline skywire, variations in the height and the length of the skywire can affect the magnitude of the anomalous tipper. The length scale over which the skywire is affecting the data is similar to the skywire height in most cases. In practice, in cases where overhead skywires cannot be avoided in field work, one could analyze some spatial requirements needed to reduce the effect of the skywire interference. As an example, for a skywire with $h =$ 25 m and $L = 500$ m, if the ground resistivity is 1000 Ωm, T_x^{max} solved from the above equation is 0.015 at $f = 1000$ Hz. In practice, equation (20) can be used to assess if the predicted tipper amplitude is within an acceptable range. Additionally, since the distorted tipper value decreases over distance away from the skywire, we can use equation (19) to estimate if we are far enough from the grounded skywire.

6. Conclusion

We have shown various examples of modeling MT using Comsol Multiphysics. For an initial model validation, we showed modeling results of the magnetotelluric response over a horizontally layered Earth and compared these with analytical solutions. Excellent agreement was found. We then showed results of the magnetotelluric response for complex crater exploration. We showed that when the uplift amplitude was 500 m and less, the uplift became difficult to detect from the resistivity profile. As seen from the modeling results, the lack of an uplift feature in the collected data indicates that the uplift in the Elbow region was probably less than 500 m in amplitude.

Last but not least, we calculated and least-squares fitted the induced current in the ground as a function of the skin depth for GIC induced in a skywire. The magnitude of the GIC was shown to decrease as a power law with respect to the normalized skin depth. We finally showed equation (20), which can be used to assess if the predicted anomalous tipper caused by GIC in the skywire is within an acceptable range.

Code availability

Comsol models presented in this paper are available at: https://drive.google.com/drive/folders/1YPZC2LgFN7hExdutH6FsI2hfSG_JlwXH?usp = sharing, hosted by Google Drive.

Credit author statement

Ang Li: conceptualization, data curation, formal analysis, investigation, methodology, software, visualization, validation, writing-original draft, writing-review and editing. S. L. Butler: conceptualization, formal analysis, funding acquisition, investigation, methodology, project administration, supervision, writing-review and editing.

Declaration of competing interest

The authors certify that they have no affiliations with or involvement in any organization or entity with any financial interest (such as honoraria; educational grants; participation in speakers' bureaus; membership, employment, consultancies, stock ownership, or other equity interest; and expert testimony or patent-licensing arrangements), or non-financial interest (such as personal or professional relationships, affiliations, knowledge or beliefs) in the subject matter or materials discussed in this manuscript.

Acknowledgements

We would like to acknowledge Phoenix Geophysics Ltd. for sponsoring the field work at Elbow and providing training for data acquisition and processing. We also like to thank Jim Merriam and Rafael Gonzalez for their efforts in the field work throughout this endeavor. We are also grateful for careful reviews by two anonymous reviewers. Last but not least, we wish to thank David Goldak for his insightful inputs to our GIC study.

References

Adepelumi, A., Fontes, S., Schnegg, P., Flexor, J., 2005. An integrated magnetotelluric and aeromagnetic investigation of the Serra de Cangalha impact crater, Brazil. Phys. Earth Planet. In.

Ansari, S., Farquharson, C., 2014. 3d finite-element forward modeling of electromagnetic data using vector and scalar potentials and unstructured grids. Geophysics 79, 149–165.

Ansari, S., Schetselaar, E., Craven, J., Farquharson, C., 2020. Three-dimensional magnetotelluric numerical simulation of realistic geologic models. Geophysics 85, E171–E190.

Bibby, J., Caldwell, T., Brown, C., 2005. Determinable and non-determinable parameters of galvanic distortion in magnetotellurics. Geophysics Journal International 163, 915–930.

Bonner, L., Schultz, A., 2017. Rapid Prediction of Electric Fields Associated with Geomagnetically Induced Currents in the Presence of Three-Dimensional Ground Structure: Projection of Remote Magnetic Observatory Data through Magnetotelluric Impedance Tensors. Space Weather. https://doi.org/10.1002/2016SW001535.

Boteler, D., Pirjola, R., 1998. The complex image method for calculating the magnetic and electric field produced at the surface of the Earth by the auroral electrojet. Geophys. J. Int. 132 (1), 31–40.

Bowles-Martinez, E., Schultz, A., 2019. The magnetotelluric method and its application to understanding geomagnetically induced currents. In: Book: Geomagnetically Induced Currents from the Sun to the Power Grid, pp. 107–126.

Butler, S., Zhang, Z., 2016. Forward modeling of geophysical electromagnetic methods using Comsol. Comput. Geosci. 87, 1–10.

Caldwell, T., Bibby, H., Brown, C., 2004. The magnetotelluric phase tensor. Geophysics Journal International 158, 457–469.

Campos-Enriques, J., Chaves-Garcia, F., Cruz, H., Acosta-Chang, J., Matsui, T., Arzate, J., Unsworth, M., Ramos-Lopez, J., 2004. Shallow crustal structure of Chicxulub impact structure crater imaged with seismic, gravity and magnetotelluric data: interfaces about the central uplift. Geophysics Journal International 157, 515–525.

Cantwell, T., Madden, T., 1960. Preliminary report on crustal magnetotelluric measurements. J. Geophys. Res. 65, 4202–4205.

Cembrowski, M., Junge, A., 2018. Electrical anisotropy in the presence of oceans–a sensitivity study. Geophys. J. Int. 213, 1029–1043.

Chave, A., Jones, A., 2012. The Magnetotelluric Method: Theory and Practice. Cambridge University Press.

Comsol, 2014. Comsol Multiphysics User's Guide. Comsol AB, Stockholm, Sweden, Version 5.0.

DeMille, G., 1960. The Elbow structure of south-central Saskatchewan. J. Alberta Soc. Petrol. Geol. 8 (5), 154–162.

Gonzalez-Castillo, L., Bohoyo, F., Junge, A., 2019. Mantle flow and deep electrical anisotropy in a main gateway: MT study in Tierra del Fuego. Sci. Rep. 9, 7148.

Gonzalez-Castillo, L., Junge, A., Galindo-Zaldivar, 2015. Influence of a narrow strait connecting a large ocean and a small sea on magnetotelluric data: Gibraltar Strait. J. Appl. Geophys. 122, 103–110.

González-Castillo, L., Galindo-Zaldívar, J., Junge, A., Martínez-Moreno, F., Löwer, A., Sanz de Galdeano, C., Pedrera, A., López-Garrido, A., Ruiz-Constán, A., Ruano, P., Martínez-Martos, M., 2015. Evidence of a large deep conductive body within the basement of the Guadalquivir foreland basin (Betic Cordillera, Spain) from tipper vector modelling: tectonic implications. Tectonophysics 663, 354–363.

Grieve, R., 2006. Impact Structures in Canada. Geological Association of Canada.

Griffiths, D., 1999. Introduction to Electrodynamics. Prentice Hall.

Hering, P., Brown, C., Junge, A., 2019. Magnetotelluric apparent resistivity tensors for improved interpretations and 3-D inversions. J. Geophys. Res.: Solid Earth 124, 7652–7679.

Hermance, J., Peltier, W., 1970. Magnetotelluric fields of a line current. J. Geophys. Res. 75, 3351–3356.

Häuserer, M., Junge, A., 2011. Electrical mantle anisotropy and crustal conductor: a 3-D conductivity model of the Rwenzori Region in western Uganda. Geophys. J. Int. 185, 1235–1242.

Ingham, M., Rodger, C., Divett, T., Dalzell, M., Peterson, T., 2017. Assessment of gic based on transfer function analysis. Space Weather 15, 1615–1627.

Jones, A., 1988. Static shift of magnetotelluric data and its removal in a sedimentary basin environment. Geophysics 53, 967–978.

Jones, A., McNeice, G., 2002. Audio-magnetotellurics (AMT) for Steeply-Dipping Mineral Targets: Importance of Multi-Component Measurements at Each Site. SEG Technical Program Expanded Abstracts 2002, p. 2478.

Keller, G., 1968. Electrical prospecting for oil. Quarterly Journal of the Colorado School of Mines 63.
Kirkby, A., Zhang, F., Peacock, J., Hassan, R., Duan, J., 2019. The MTpy software package for magnetotelluric data analysis and visualisation. Journal of Open Source Software 4, 1358.
Krieger, L., Peacock, J., 2014. MTpy: a python toolbox for magnetotellurics. Comput. Geosci. 72, 167–175.
Li, A., 2020. Magnetotelluric Study of the Saskatchewan Elbow Impact Structure and Applications of Finite-Element Modeling. Department of Geological Sciences, University of Saskatchewan. Master's thesis.
Liu, Y., Junge, A., Yang, B., Lower, A., Cembrowski, M., Xu, Y., 2019. Electrically anisotropic crust from three-dimensional magnetotelluric modeling in the Western Junggar, NW China. J. Geophys. Res.: Solid Earth 124, 9474–9494.
Lower, A., Junge, A., 2017. Magnetotelluric transfer functions: phase tensor and tipper vector above a simple anisotropic three-dimensional conductivity anomaly and implications for 3D isotropic inversion. Pure Appl. Geophys. 174, 2089–2101.
Mareschal, M., Chouteau, M., 1990. A magnetotelluric investigation of the structural geology beneath Charlevoix Crater, Quebec. Phys. Earth Planet. In. 60, 120–131.
Masero, W., Fischer, G., Schnegg, P., 1997. Electrical conductivity and crustal deformation from magnetotelluric results in the region of the Araguainha impact, Brazil. Phys. Earth Planet. In. 101, 271–289.
Masero, W., Schnegg, P., Fontes, S., 1994. A magnetotelluric investigation of the Araguainha impact structure in Mato Grosso-Goias, central Brazil. Geophys. J. Int. 116, 366–376.
Matandirotya, E., Cilliers, P., Van Zyl, R., 2015. Modeling geomagnetically induced currents in the South African power transmission network using the finite element method. Space Weather 13, 185–195.
McLeod, J., 2016. Magnetotelluric and Controlled-Source Electromagnetic Pre-injection Study of Aquistore CO2 Sequestration Site, Near Estevan, Saskatchewan, Canada. Master's Thesis. Clayton H. Riddell Faculty of Environment, Earth, and Resources. Department of Geological Sciences, University of Manitoba, Winnipeg.
McNeill, J., Labson, V., 1991. Geological mapping using vlf radio fields. In: Nabighian, M.N. (Ed.), Electromagnetic Methods in Applied Geophysics. Society of Exploration Geophysicists, Tulsa, Oklahoma 2, pp. 521–587.
Oliveria, D., Ngwira, C., 2017. Geomagnetically induced currents: principles. Brazalian Journal of Physics 47 (5), 552–560.
Phoenix, 2019. Empower Data Management.
Pilkington, R., Grieve, R., 1992. The geophysical signature of terrestrial impact craters. Rev. Geophys. 30 (2), 161–181.
Pirjola, R., 1998. Series expansions for the electric and magnetic field produced by a line current source. Radio Sci. 33, 33–38.
Pirjola, R., Boteler, D., 2002. Calculation methods of the electric and magnetic fields at the earth's surface produced by a line current. Radio Sci. 37, 1042.
Pirjola, R., Vilijanen, ., 1999. Series expansions for the electric and magnetic fields produced by a line or sheet current source above a layered earth. Radio Sci. 34, 269–280.
Pirjola, R., Vilijanen, A., 1998. Complex image method for calculating electric and magnetic fields produced by an auroral electrojet of finite length. Ann. Geophys. 16 (11), 1434–1444.
Queralt, P., Jones, A., Ledo, J., 2007. Electromagnetic imaging of a complex ore body: 3D forward modeling, sensitivity tests, and down-mine measurements. Geophysics 72, 85–95.
Simpson, F., Bahr, K., 2005. Practical Magnetotellurics. Cambridge University Press.
Swift, C., 1967. A Magnetotelluric Investigation of an Electrical Conductivity Anomaly in the South-Western United States. PhD Thesis. Massachusetts Institute of Technology, Cambridge, MA, U.S.A.
Telford, W., Geldart, L., Sheriff, R., 1990. Applied Geophysics, second ed. Cambridge University Press.
Unsworth, M., Enriques, O., Belmonte, S., Arzate, J., Bedrosian, P., 2002. Crustal structure of the Chicxulub Impact crater imaged with magnetotelluric exploration. Geophys. Res. Lett. 29 (16), 35–1–35–4.
Van der Vorst, H., 1992. Bi-CGSTAB: a fast and smoothly converging variant of Bi-CG for the solution of nonsymmetric linear systems. SIAM J. Sci. Stat. Comput. 13, 631–644.
Vozoff, K., 1991. The magnetotelluric method. In: Nabighian, M.N. (Ed.), Electromagnetic Methods in Applied Geophysics, vol. 2. Society of Exploration Geophysicists (part B).
Wait, J., 1981. Wave Propagation Theory. Pergamon Press, New York.
Witherly, K., Goldak, D., Kosteniuk, P., 2010. An Assessment of EM and Potential Field Data at Pasfield Lake, Saskatchewan - a Suspect Astrobleme. Society of Exploration Geophysicists, Denver 2020 Annual Meeting.
Zhang, P., Rasmussen, T., Pedersen, L., 1988. Electrical resistivity structure of the Siljan impact region. J. Geophys. Res. 93, 6485–6501.
Zhdanov, M., Varentsov, I., Weaver, N., Golubev, N., Krylov, V., 1997. Methods for modelling electromagnetic field results from commeni - the international project on the comparison of modelling methods for electromagnetic induction. J. Appl. Geophys. 133–271.